INT. J. REMOTE SENSING, 1981, VOL. 2, NO. 2, 155–183

A radar image time series

F. LEBERL and H. FUCHS

Technical University Graz, Austria

J. P. FORD

Jet Propulsion Laboratory, Pasadena, U.S.A.

(*Received 3 January 1980; revision received 14 July 1980*)

Abstract. A set of side-looking radar images has been collected over an area in the Sierrita Pediment, Arizona, U.S.A. The dates of image acquisition vary from 1965–1979 and the images are taken at various look angles, frequencies, flight directions and polarizations. The objective of the study is to demonstrate the photogrammetric orthophoto technique applied to radar images and at the same time to study the characteristics of this unique set of radar images taken over the same area by many different sensors. Ten images are presented here, of which five have been rectified using ground control points and a digital height model taken from a map. Errors prior to rectification are shown to amount to several hundred metres on the ground in all cases; after rectification, residual coordinate errors in ground control range from ±19 m to ±70 m. The contents of the radar images, including one pass from Seasat, were compared with a Landsat image and aerial photography. Observations made confirm a range of conclusions on the effect of system parameters on the radar image. The data set also permitted a unique review of changes that occurred in the area over time, and of variations in radar performance as a function of some system parameters.

1. Introduction

Radar images of the earths surface represent a look with 'alien eyes' (Kobrick 1980) and are not well understood. The effects of look-angle, frequency of electromagnetic radiation, type of radar, flight direction, etc., are all factors still needing intensive study (Radar Geology Workshop 1979). Although side-looking radar (SLR) images have been used for cartographic research since at least about 1964 (Matthews 1975), actual mapping applications have consisted essentially of reconnaissance type, quick-look radar coverages of large areas. In the interest of timeliness these surveys did not resort to advanced radargrammetric solutions. Research work on mapping from SLR images has generally been confined to very limited data sets, the purpose often being the analysis of errors in a single radar image. This means that, although a considerable body of literature on radargrammetry exists (Leberl 1976) further study is still required.

The general lack of data motivated the collection of a unique set of 14 SLR images over one area in Arizona, U.S.A. about 30 km south-west of Tucson, in the Sierrita–Twin Buttes–Pima Mining District. The data were acquired with a variety of radar imaging systems over a period of 14 years, from 1965 to 1979, but none of the images was acquired for the purpose of this study. The availability of collateral information on the radar system parameters that were used at the time of data acquisition varies widely. Though details of the respective imaging geometries and

0143–1161/81/0202 0155 $02·00

wavelengths are available it is impossible to compare or contrast the information content in the images with respect to the different grey-level values due to the absence of any standard of calibration. However, the images reveal a varied complexity of natural and man-made surfaces in a major open-pit mining area in the arid semi-desert of south-east Arizona. They show stages of development in the mines and present a record of changes in the area. Of more interest are the changes from image to image that are system dependent.

The study has two main goals

(*a*) to evaluate and demonstrate the use of a photogrammetric optical projector for the differential rectification of radar images using ground control points and a digital height model;

(*b*) to present and study an image time series of one small area, thereby comparing sensors and sensor parameters to the extent feasible.

Initially only five images were available and their geometry differentially rectified so that radar orthophotos were produced. The existence of other radar images of the area was discovered later, so that a total of fourteen images became available. However, a limitation of resources for the study did not permit the rectification of all the images. Also the data are partly redundant so that we are presenting here only ten images.

While the data are well suited for the first objective of the study, the second is hampered by the lack of detailed information on the system parameters used for imaging. Only cursory information is available on the historic images dating back to 1965.

2. Description of the imaged area

The ground surface of the imaged area slopes uniformly to the east, and exposes mostly medium-to-coarse-grained alluvial gravels of recent geologic age. The alluvial deposits are derived by erosion and mass wastage of granitic and other rocks in the Sierrita Mountains to the west. The eastward slope is about 25 m/km, which coincides with an eastward thickening of the alluvial cover from less than 30 m at Helmet Peak in the west to over 300 m at Sahuarita in the east (estimates of thickness from Cooley (1973)). Bedrock exposures are remarkably few. They consist of several small knolls and hills, the most notable of which are Twin Buttes, Helmet Peak and Mineral Hill. Figure 1 shows a sketch map as derived from one radar image. Major geologic structure is not evident in the small area imaged.

Vegetation cover is open and widely spaced, and has been extensively disturbed by large-scale open-pit mining. West of the Santa Cruz valley the natural vegetation belongs predominantly to the paloverde-saguaro community of the Sonoran Desert (Turner 1974). The community forms a complex of small trees such as foothills paloverde, and shrubs such as creosotebush, and several species of cactus. The southwest portion of the imaged area is typically grassland that has been invaded by shrubs such as mesquite. The eastern margin of the area is marked by cultivation in the bottom lands of the Santa Cruz valley.

Drainage channels are incised downslope into the alluvial gravels, and oriented eastward to the Santa Cruz River. All channels are dry. The only surface water present in the area is in man-made tailings ponds. Routeways and roads in the area consist of the major Tucson–Nogales Interstate Highway (I–19) and the Southern Pacific Railroad, both of which parallel the Santa Cruz valley, and east–west access roads to mines and adjacent small communities or ranches.

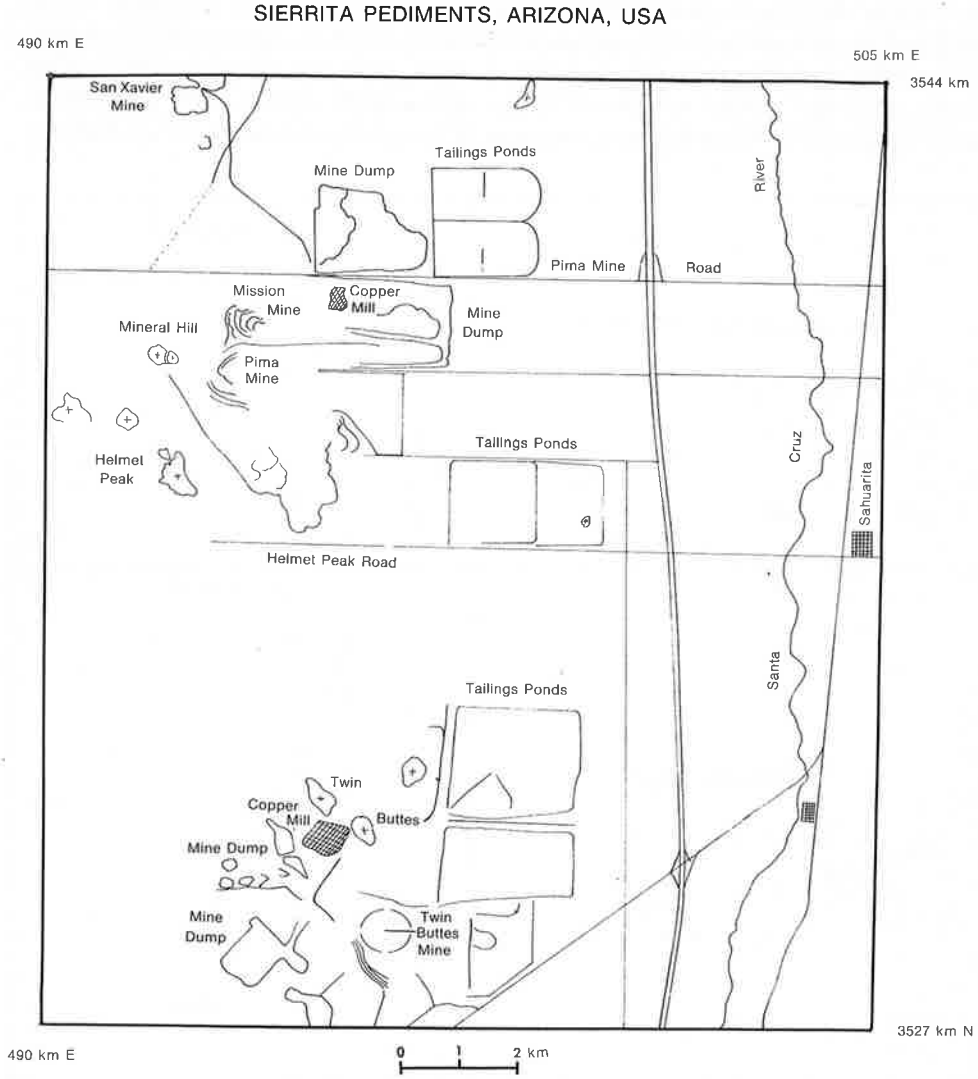

Figure 1. Sketch map of the study area in Arizona, U.S.A., prepared from the X-band Goodyear–GEMS image of 1973 (compare figure 9).

The Mining District contains the first mining claims in the Arizona Territory. By 1961 the District started to be a leading U.S. copper producer. In the mid-1970s production values for the entire District averaged one-quarter billion dollars annually. Mines in the imaged area include the San Xavier, Mission, Pima, and Twin Buttes (figure 1). Pay zones in the mines are covered by tens of metres of alluvial overburden which has been and is being stripped and dumped on the adjacent land. For example, stripping of the Twin Buttes copper deposit started in 1965. Total material removed during the first 10 years of operation of that mine was approximately 800 million metric tons.

3. Collected images and collateral data

As a result of mining activities, the Sierrita Pediment has been covered repeatedly

by various imaging missions. The collected total of radar images was taken in five different aircraft missions and one pass of the Seasat synthetic aperture radar satellite. The radar system parameters for the missions and data are given in table 1. Some of the radar coverages consist of several images where flight direction (Westinghouse), polarization (JPL, Westinghouse), and type of processing (Seasat) is varied. Figure 2

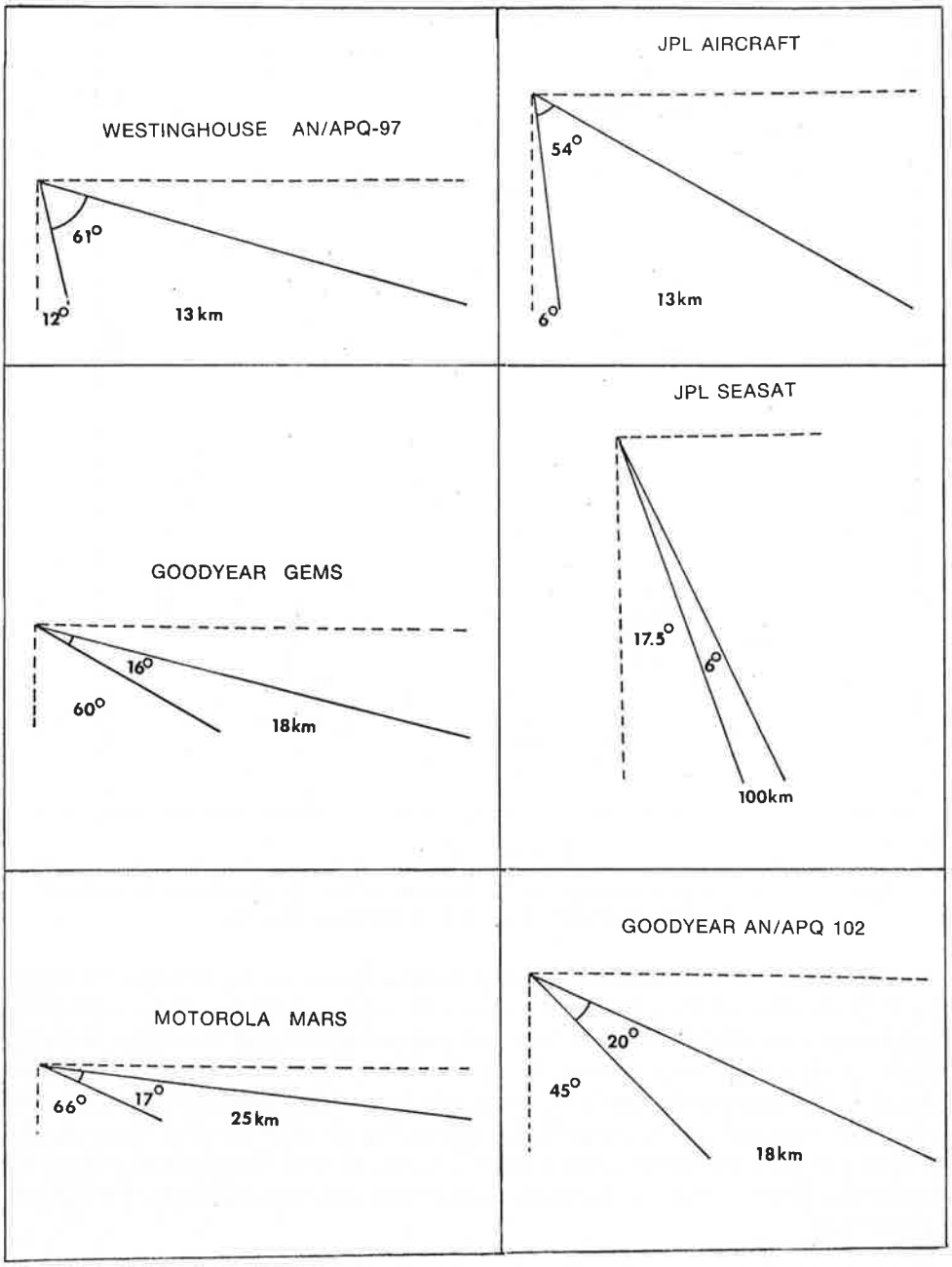

Figure 2. Radar beam geometries for the radar system used to generate the images of figures 6–9 and 12–17.

Table 1. Parameters of presented radar imagery†. The indicated look-angles are average values for the image.

Figure	Designation of image	Real/synthetic aperture	Resolution (nominal)	Flight height	Date	Approximate wave-length	Average look-angle off Nadir	Remarks
7	Westinghouse A	Real (AN/APQ 97)	20–30 m	6 km	1965	0·8 cm	40°	North–South cross-polarized
8	Westinghouse B	Real (AN/APQ 97)	20–30 m	6 km	1965	0·8 cm	40°	East–west cross-polarized
6	Westinghouse C	Real	20–30 m	6 km	1965	0·8 cm	40°	North–south like-polarized
9	Goodyear–GEMS	Synthetic	12 m	12 km	1973	3 cm	68°	
12	Motorola	Real			1975	3 cm	74°	
13	Jet Propulsion Laboratory (JPL) A	Synthetic	25 m	10 km	1977	25 cm	33°	Cross-polarized
14	Jet Propulsion Laboratory (JPL) B	Synthetic	25 m	10 km	1977	25 cm	33°	Like-polarized
17	Johnson Space Center (JSC), AN/APQ 102	Synthetic	10 m	20 km	1979	3 cm	55°	Optical correlation like-polarized
15	Seasat A	Synthetic	30 m	800 km	Aug. 1978	25 cm	20°	Optical correlation
16	Seasat B	Synthetic	30 m	800 km	Aug. 1978	25 cm	20°	Digital correlation

† Not presented, but also available are a like-polarized version of the Westinghouse B image, a cross-polarized version of the JSC-image, and two more images from the Motorola-system overlapping the one presented here.

shows elevation diagrams of the radar imaging geometries that were used to acquire the radar images in figures 6–9 and 12–17 respectively. There are significant differences in the look angle, beamwidth and swathwidth of each of the imaging systems. The look angle is measured between the vertical plane and a line that links an imaging radar antenna to a feature on the ground. The beamwidth defines the angular coverage of the radar beam in a vertical plane at the antenna. The swathwidth is a measure of the linear ground distance that is covered from near range to far range in the direction of the radar scene-illumination. For a given target area and a given direction of scene-illumination the combination of look angle, beamwidth and swathwidth used on any imaging radar system has a pronounced effect on the character and extent of the geometric distortion that is present on the radar image acquired with that system. The rectification geometry of the images analyzed here is presented in §6, and the thematic content of the images is described in §7.

The area is also covered by Landsat Multispectral scanner (MSS) and aerial photography. These provide information on the thematic contents of the radar data. We include a Landsat MSS image subscene of band 7 as figure 19, and a section of a small scale aerial photograph taken at scale 1:130 000 as figure 18.

For the rectification of the five radar images control points were identified and scaled off the topographic maps at scale 1:62 500 or, where available, at scale 1:24 000, and also off orthophoto maps at scale 1:24 000. The available maps are of different age and many of the features from the radar data are not shown in the maps so that control point identification was a difficult problem.

4. Computation of radar image deformations

The basic radargrammetric projection equations have been extensively documented in the literature and were reviewed, for example, by Leberl (1976). The technique for differential rectification of SLR images has been described in a separate paper (Leberl and Fuchs 1978). A summary of the method to compute radar image deformations using control points is presented in Appendix A.

5. The rectification process

5.1. *The rectifier*

A modern, computer-controlled photogrammetric rectifier can employ the same input on image deformation as is used for rectification with digital image processing. An example of such an instrument is the Avioplan OR 1, produced by Wild of Heerbrugg (Switzerland). This was the instrument used in this project.

Figure 3 illustrates the principle of differential rectification. Figure 3 (*b*) is the rectangular mesh of orthophoto points in the rectified image; the corresponding points in the original image form a distorted grid (figure 3 (*a*)). The orthophoto instrument is capable of converting the deformed grid into the rectangular format. For this it is necessary to present the rectifier with a magnetic tape containing the x, y coordinates of the distorted grid points in the image. The new, rectified image is obtained by sequentially profiling in the orthophoto plane, for example in the y-direction, using a slit as wide as the grid mesh size. The image contents are projected on to the orthophoto plane in such a way that the distorted grid is converted to the regular one. This is the usual principle of orthophoto production as described in handbooks on photogrammetry (for example, Manual of Photogrammetry 1966). It is stressed that in digital image processing such a rectification procedure is denoted

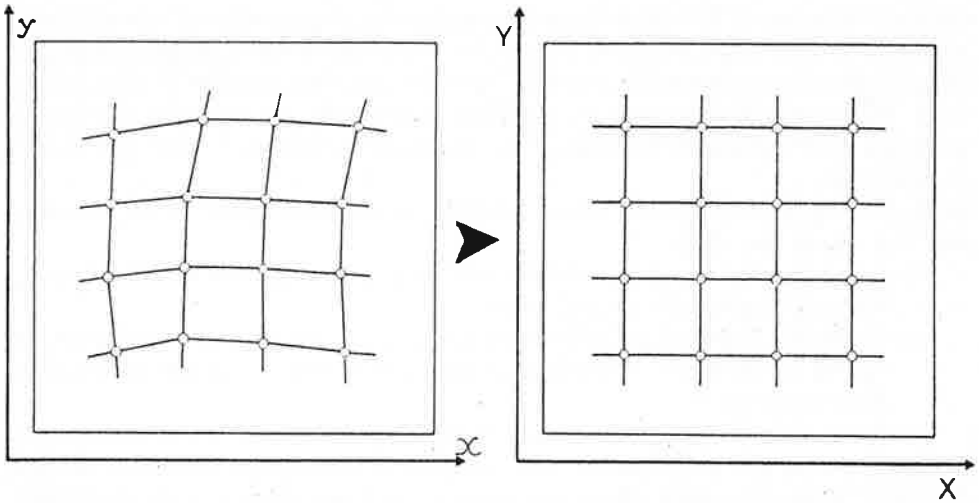

Figure 3. Principle of rectification for a computer controlled photogrammetric orthophoto-instrument: any distorted grid can be rectified to fit a regular square grid (from Kraus 1976).

by 'resampling' or 'indirect method of rectification' (compare, for example, Konecny 1979).

5.2. *Input to the rectifier*

The image deformations in control points are computed according to Appendix A, equation (A 14). Then the input for rectification is generated. For each of the regularly spaced orthophoto grid points one needs to compute the corresponding image point.

For this purpose the position vector in object space, **g**, for each grid point is used to determine the corresponding x_b, y_b-coordinates. This relies on the same formulae as those used for control points (equations (A 4) through (A 12)); then corrections Δx, Δy are applied to the preliminary x_b, y_b values employing equation (A 14). The result of this operation is a list of x, y image coordinates of the distorted grid that correspond to the regular grid points in the orthophoto.

5.3. *Digital height model*

The position vector, **g**, of the grid points requires that both horizontal as well as vertical coordinates of a point be available. Horizontal coordinates derive from the grid mesh size which in turn is defined by the length of the profiling slit for orthophoto production. Vertical coordinates, or terrain heights, must be measured. In the present case this was done off topographic maps at scale 1:62 500, and 1 : 24 000, with 50 ft (15 m) contour lines. However, any other source of height coordinates would be usable, for example, from stereoradar.

5.4. *Errors of the orthophoto*

The orthophoto may still have geometric defects. This is a result of two types of limitations

(*a*) control point density and identifications;

(*b*) orthophoto system limitations.

ad (*a*): Difficulties in identifying control points in both the image and a map limit the

orthophoto accuracy. This is also a problem with aerial photographs but is much more pronounced with radar. Due to the kinematic (dynamic) mode of image acquisition, image geometry is comparably unstable. Therefore accuracy depends on the number or density of ground control points available in an image, and of course also on the precision of identifying these points. There is extensive evidence to support this fact (Leberl 1976).

ad (*b*): Orthophoto system limitations result from the finite length of the scanning slit. This causes two effects:

(i) the systematic, non-linear deformations are in fact approximated by linearly interpolating in between grid points;

(ii) the height of the terrain in between grid points is not known: terrain may in fact be curved where orthophoto production assumes a surface composed of plane elements.

We have analysed the order of magnitude of system errors (Leberl and Fuchs 1978) and found that class (i) errors are negligible in comparison with those of class (ii). Only terrain curvature effects can reach a size large enough to be significant. Figure 4 presents the effect of terrain curvature. However, where terrain curvature is large, there normally exists the additional problem that control points are difficult to be identified: hence larger orthophoto errors must be accepted in rugged terrain as compared with flat, cultivated areas.

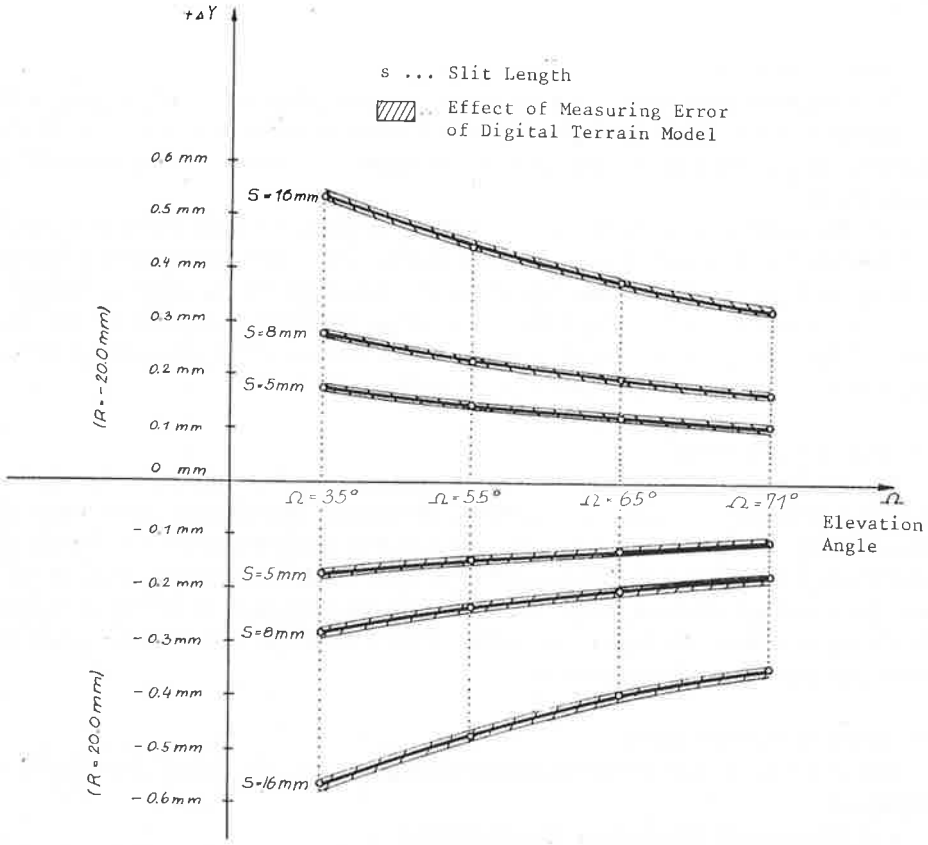

Figure 4. Effect of neglected terrain curvature on the geometry of the radar orthophoto. R = radius of curvature of the terrain.

6. Results of differential rectification

6.1. *Accuracy*

Table 2 presents an overview of the geometrical errors encountered in the five rectified images, before and after the rectification. The rectification process was designed to transform the images to the map using map-derived control points. Hence it was *not* the main purpose to register the images. This point is stressed because only such control points were used that could be identified in the map. The control point distribution is presented in figure 5. Not all points were identifiable in all images. There are image areas where no map points could be located, as is the case, for example, in the eastern portion of the Westinghouse data (compare figures 6 and 7). Hence the images may exhibit geometrical differences even after rectification. Had one aimed at image registration, then rectification would be based on points that can be identified in both images, irrespective of their significance in a map. As a result one would not encounter discrepancies between two images, but they could *both* still be deformed.

Table 2. Root mean square coordinate errors (metres) in control points in the five rectified radar images, computed after a scale fit of each image, after affine corrections, and after rectification.

Image	Before rectification scale fit		Affine correction		Scale difference along versus across flight direction (per cent)	After rectification		Number of control points	Density points/ 100 km²
	x	*y*	*x*	*y*		*x*	*y*		
Westinghouse A	315	432	288	226	19	59	27	19	9·1
Westinghouse B	288	317	164	125	16	45	19	16	8·7
Goodyear–GEMS	157	408	44	54	18	40	18	21	6·4
Motorola	130	210	66	84	6	52	52	24	6·4
Jet Propulsion Laboratory A	110	128	107	45	8	99	45	8	8

All the raw images exhibited a significant difference between along- and cross-track scale, ranging up to nearly 20 per cent. This highlights the well-known difficulty in obtaining original radar imagery of good geometric quality: the dynamic mode of imaging, and the independence of along- and cross-track dimensions can be a source of geometric deformations. However, in the two ground range presentations that exist among the ten radar images (Goodyear and Motorola, figures 9 and 12 of §7), the main errors can be described by an affine transformation where map coordinates E, N result from image coordinates *x*, *y* as follows:

$$\left.\begin{aligned} \mathrm{E} &= a_1 + a_2 x + a_3 y \\ \mathrm{N} &= b_1 + b_2 x + b_3 y \end{aligned}\right\} \qquad (1)$$

Equation (1) is a gross simplification of the more rigorous transformation of Appendix A.

Using a more complex transformation than a mere affine correction one finds distinct accuracy improvements only in the Westinghouse images, which originally exhibited a slant range presentation (figure 6).

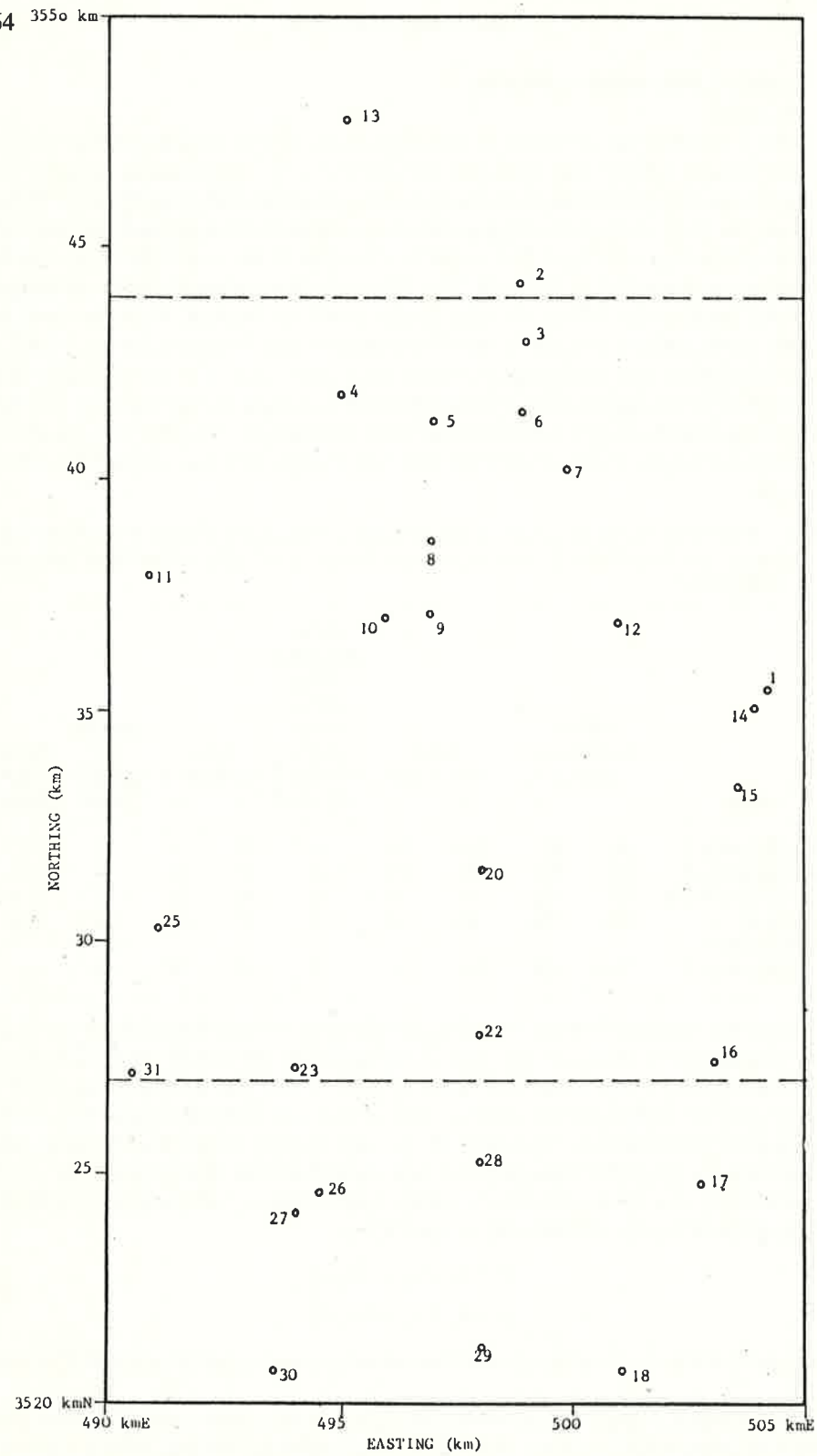

Figure 5. Distribution of control points used for the rectification.

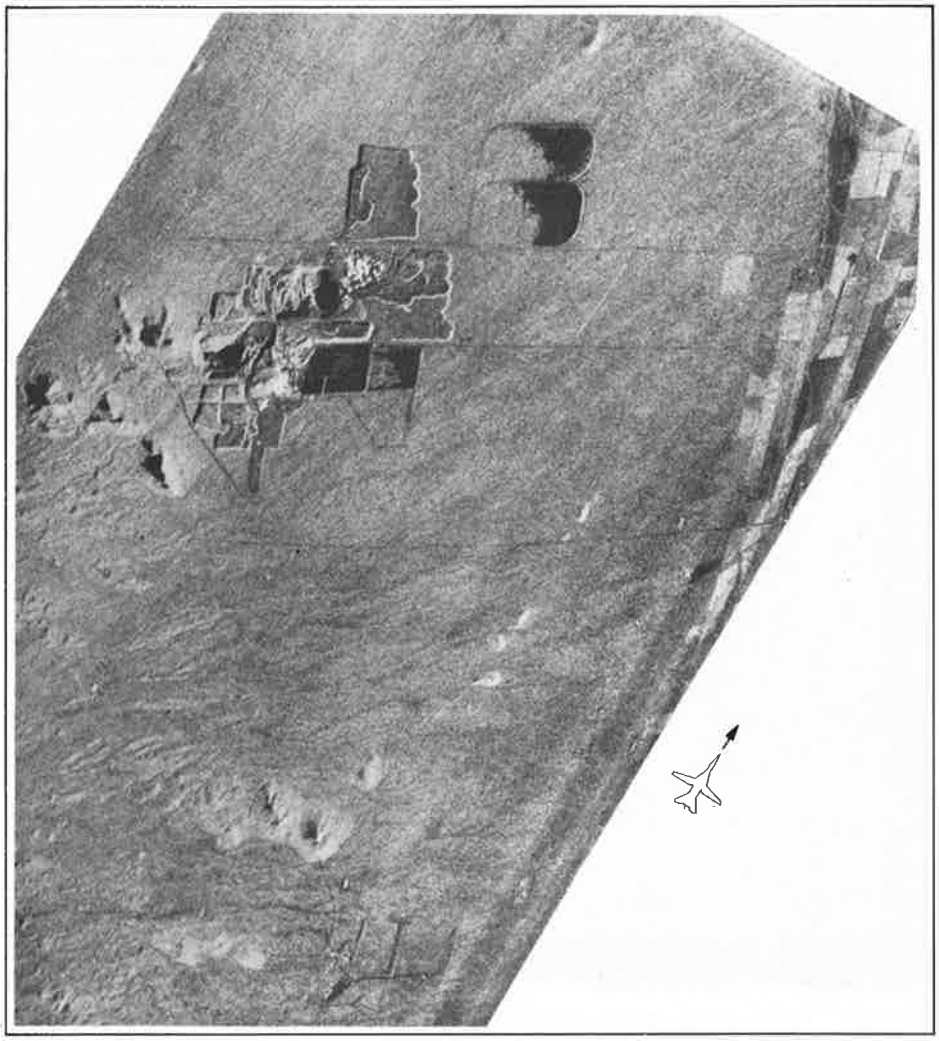

Figure 6. Real aperture SLR image of Westinghouse (1965), unrectified, slant range presentation. Like-polarized, imaging to the east. Compare with figure 7 for effect of rectification. Ka-band (0·8 cm).

Residuals in control points are smaller in cross-track or range-direction than in flight- or azimuth-direction. This confirms earlier observations with aircraft real-aperture radar (Leberl 1976). The effect could be caused by irregular antenna yaw affecting only azimuth coordinates, by a reduced resolution in azimuth as compared with range, and by variations in the antenna tip angle.

In the case of JPLs L-band radar (figure 13), a cross-polarized image was available with little contrast. Point identification was particularly difficult: only a few control points could be found and their identification in the image was not very reliable. As a result, residual errors are comparatively large. The accuracies achieved with the JPL-radar conform with earlier results as reviewed by Leberl (1976).

6.2. *The ortho-images*

The five orthophotos were produced at scale 1:62 500 and hence were enlarged

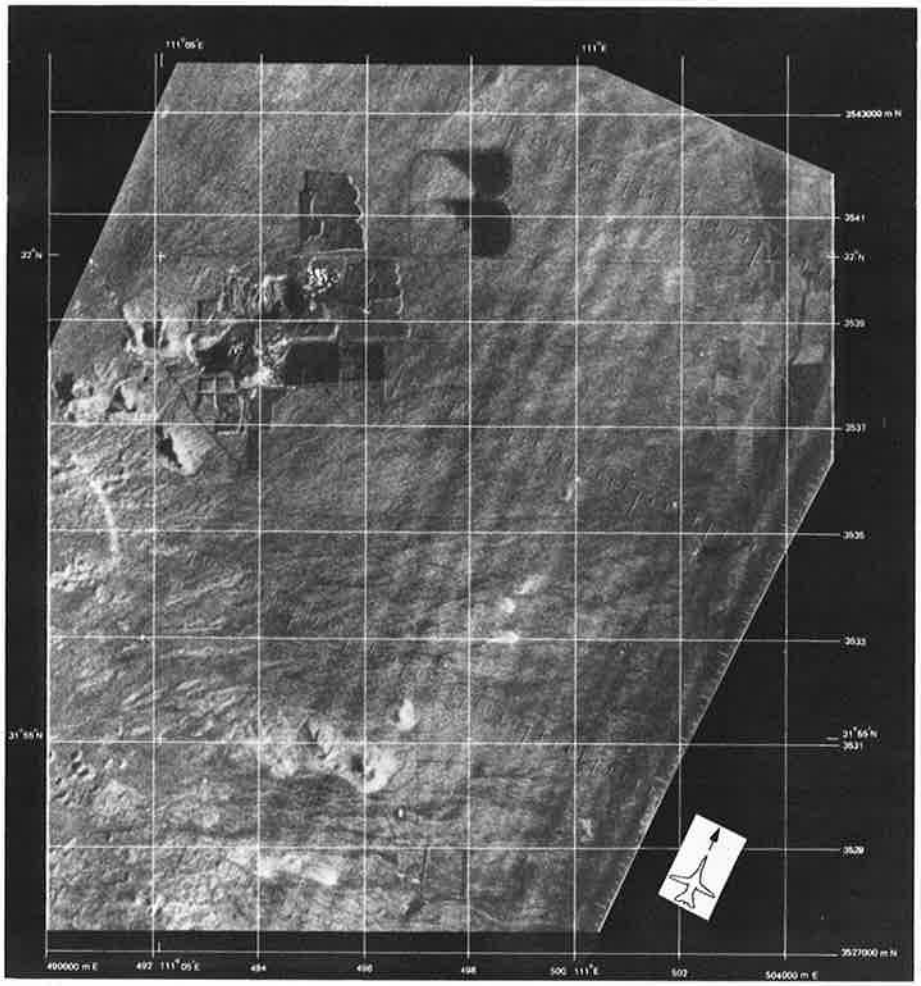

Figure 7. Real aperture SLR image of Westinghouse (1965), rectified to UTM projection. Cross-polarized, imaging to the east. Ka-band (0·8 cm).

from their original scale. An example of the original image and the differentially rectified result is presented in figures 6 and 7. It should be noted, however, that the image of figure 6 is of different polarisation from that of figure 7.

Slit length for profiling was selected as 8 mm, typical of many conventional orthophoto projects. At the orthophoto scale 1:62 500 this corresponds to 500 m on the ground. At the original image scale, for example of the Westinghouse image of figures 6 and 7, of 1:200 000, the slit length corresponds to 2·5 mm. Some raw data, however, were at scale 1:400 000, so that here the slit length in the original image corresponds to 1·25 mm.

The rectified images are shown in figure 7 and in figures 8, 9 and 12, 13 of §7.

7. Thematic analysis of image contents

Ten selected radar images, one high-altitude aerial photograph, and one Landsat multispectral scanner image (band 7) of the study area are presented here (figures 6–9 and 12–19), and compared with respect to image content. The radar images are

arranged sequentially in order of their acquisition from 1965 to 1979. The imaging geometry used in each of the six different radar systems with which the respective images were acquired is sketched in figure 2.

In general the maximum geometric distortion due to relief in a radar image occurs at a low look-angle. Low look-angles also display the strongest image deformation if slant ranges are displayed. This can be seen especially in the near range on the unrectified Westinghouse AN/APQ–97 (figure 6), the near range on the unrectified JPL aircraft image, and on the unrectified Seasat SLR images (figures 15 and 16). Geometric distortion is reduced when ground ranges are displayed and when a high look-angle is used, as on the Goodyear GEMS, Goodyear AN/APQ–102 (see unrectified image, figure 17), and Motorola radar systems.

The degree of geometric distortion is non-uniform across an image from the near range to the far range. This effect is most noticeable with imaging systems that have a wide beamwidth, and a low look-angle in the near range (for example, Westinghouse, figure 6; JPL aircraft, figure 14). The geometric distortion of relief on land surfaces on Seasat SLR images is generally large due to the very low look-angle of the system. The distortion is essentially uniform across the wide swath because of the narrow beamwidth and the orbital altitude at which the images were acquired (figures 14 and 15).

7.1. *Radar image of 1965, real-aperture Ka-band*

Figure 6 (unrectified) and figures 7 and 8 (rectified) present Westinghouse AN/APQ–97 Ka-band real-aperture like-polarized and cross-polarized images of the area. They were taken in 1965 in the context of early NASA radar-mapping studies. The like-polarized image (figure 6) has the wider range of brightness values (see the area near the flight line), but buildings and bench-cuts in the mines produce stronger radar returns which result in saturation and obscuring of detail. The saturation effects are slightly less pronounced on the cross-polarized images. Radar resolution is nominally 12 m in the range direction, but 30 m in azimuth so that an average of 20–30 m is listed in table 1.

The images were acquired when stripping operations at the Twin Buttes mine had just commenced (November 1965). The position of the mine excavation and the layout of dump sites and tailings ponds are clearly evident on all images. A generally north-east orientation of the small bedrock hills that protrude above the alluvial surface cover is likewise clear. Bright radar returns from the dumps at the Pima and Mission mines come from steep slopes that face the radar look-direction; obviously no returns come from slopes that are in radar shadow. Drainage channels are highlighted by bright image tones; roads and access ways to the mines appear dark. Cultivation patterns are clear in the Santa Cruz valley to the east with only slight loss of contrast in the cross-polarized as compared with the like-polarized images. The along-track bands on the images are system artefacts that represent uneven CRT illumination in the image generation.

7.2. *Radar image of 1973, synthetic-aperture X-band*

The Goodyear (GEMS) X-band synthetic-aperture radar imagery of figure 9 was taken with a stabilized antenna. The image is sharper than the older Ka-band data of 1965 although it has slightly lower image contrasts and shows the speckle that is characteristic of all synthetic-aperture imagery.

Mine dumps and tailings ponds cover 2–3 times the area occupied on the images

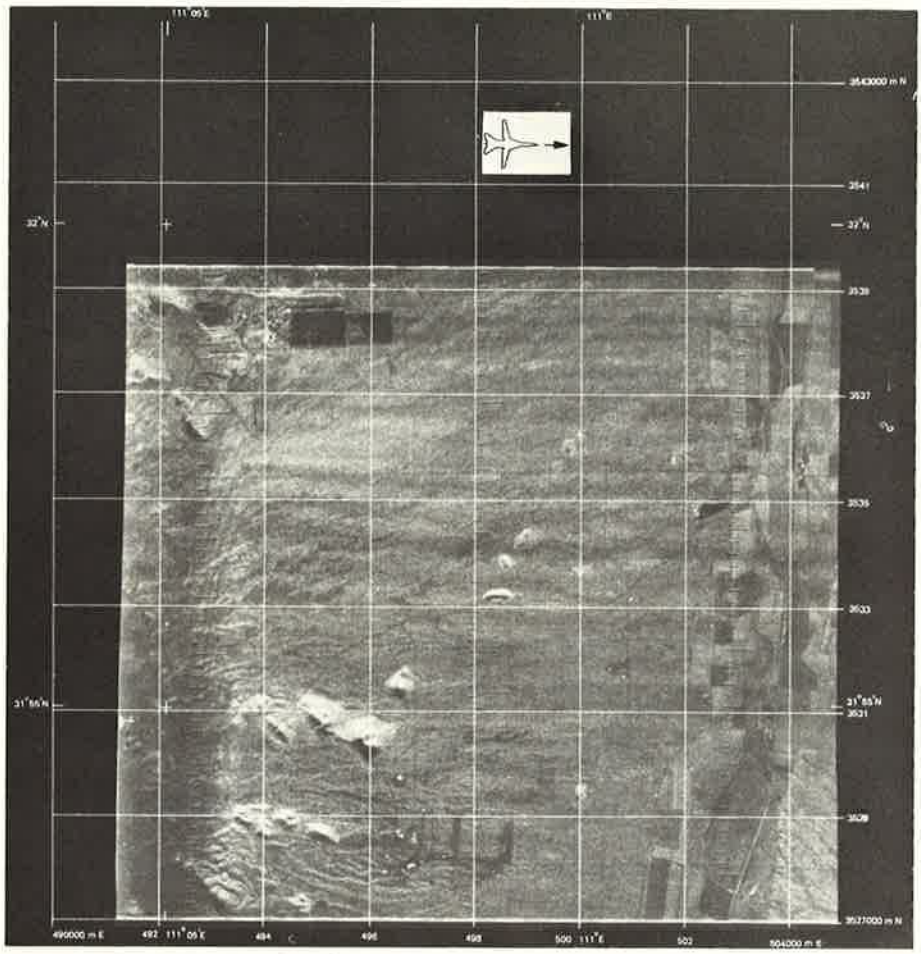

Figure 8. Real-aperture SLR image of Westinghouse (1965), rectified to UTM projection. Cross-polarized, imaging to the south. Ka-band (0·8 cm).

taken in 1965. Tailings ponds have so encroached upon the landscape that north-east-oriented hills above the alluvial cover seen clearly in the 1965 images (figures 6–8) are no longer so clearly evidenced in the 1973 image. The north-eastern most hill is totally surrounded by a tailings pond. Substantial growth at Twin Buttes Mine includes excavation of a large pit shown in the lower centre of figure 9; figure 10 is a photograph taken from the south-east edge. The growth also includes extensive ponds and dumps, and construction of numerous buildings including a copper mill immediately south of and adjacent to the buttes. Steep slopes of the Mission Mine pond north of Pima Mine Road that are responsible for bright radar returns on the imagery are also shown in a photograph (figure 11). Bright returns are likewise evident on the imagery from steep slopes of all dumps and ponds which face the radar look-direction. Drainage channels appear bright and more distinct. The new Tucson–Nogales Interstate Highway which did not exist in 1965 appears as a dark narrow ribbon from north to south on the right side of the image, due to specular reflection on the asphalt (figure 9). Bright specular returns to the antenna come from overpass and underpass bridges along the highway and from traffic on the highway. Roads

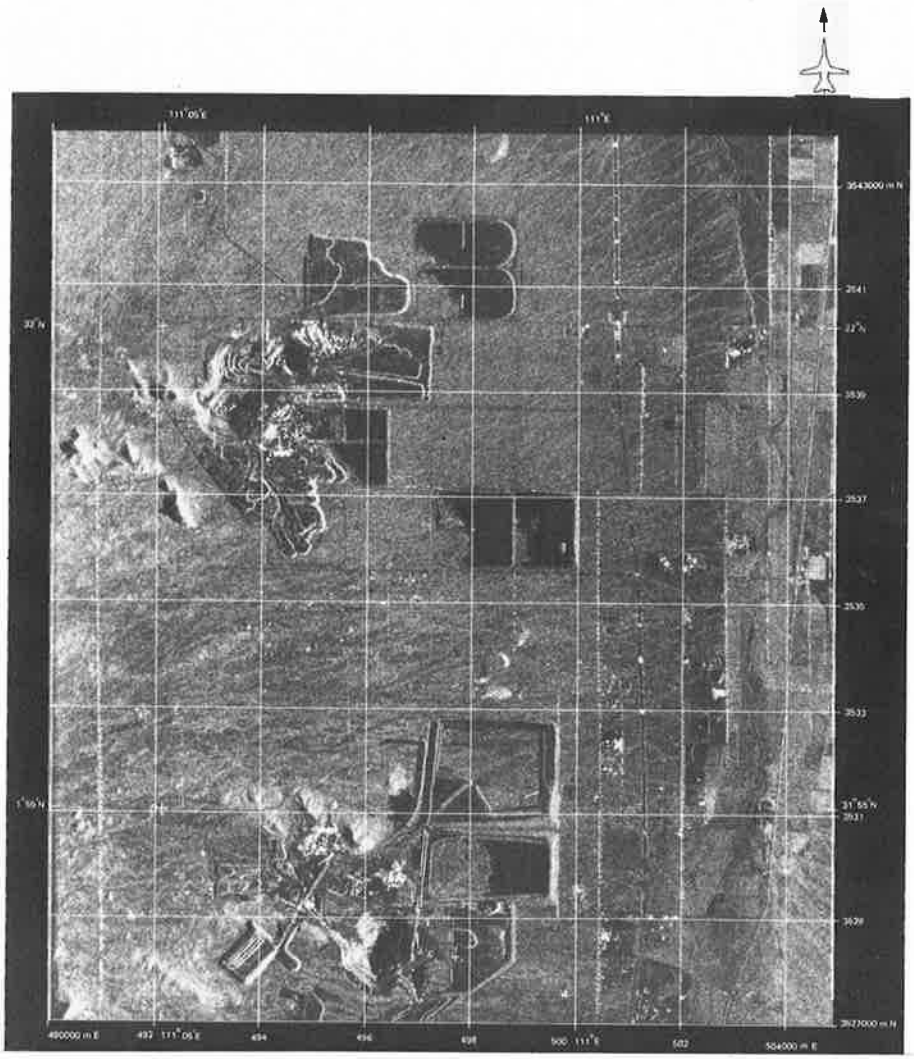

Figure 9. Synthetic aperture SLR of Goodyear–GEMS (1973), rectified to UTM projection. Imaging to the west. X-band (3 cm). Optical correlation. (Courtesy Aeroservice–Goodyear.)

that are parallel to the along-track direction are clearly denoted by successions of bright returns from point targets (cars, transmission towers) along the respective way. Figure 9 covers the entire study area and shows also the new San Xavier Mine in the north-west.

7.3. *Radar image of 1975, real-aperture X-band*

The X-band real-aperture radar imagery of August 1975 was taken with a Motorola radar system (figure 12). The high look-angle creates shadows from Twin Buttes and Helmet Peak, etc., that are longer than in figure 9. Image contrast is greater than with SAR and speckle is absent from the real-aperture imagery. Point-target bright reflections from roads that parallel the along-track direction are not present (cf. figure 9). The geometric resolution of the image is not representative of the performance capability of the system. However, no better data are available from that point in time.

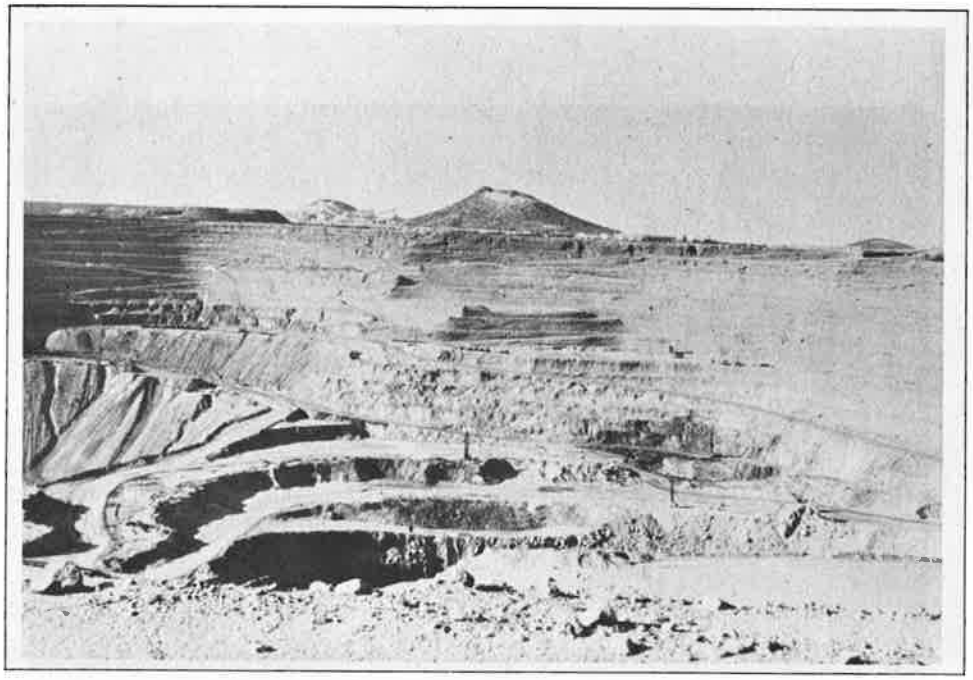

Figure 10. Photograph (ground truth) of open pit at Twin Buttes Mine as seen from the south-east edge looking north-west.

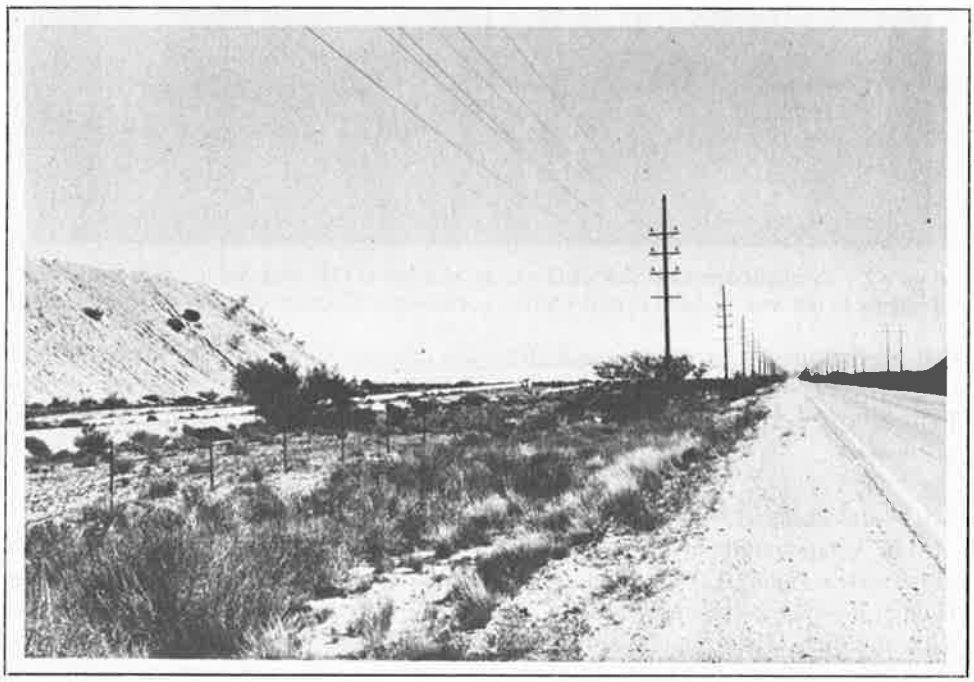

Figure 11. Photograph (ground truth) of the steep slope at the south-eastern rim of the Mission Mine pond north of Pima Road. Photograph looking east.

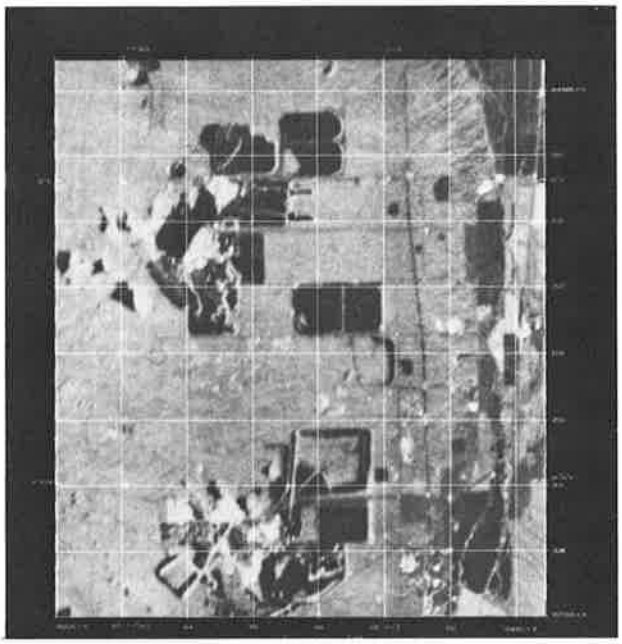

Figure 12. Real aperture SLR of Motorola (1975), rectified to UTM projection. Imaging to the west. X-band (3 cm). (Courtesy of Motorola Aerial Remote Sensing.)

Notable contrasts in the area from 1973 to 1975 that appear on the imagery consist of extensions to the Mission Mine dump south of Pima Mine Road, construction of an additional tailings pond south of Helmet Peak Road, and enlargement of the mine dump west of the Twin Buttes pit.

7.4. *Radar image of 1977, synthetic-aperture L-band*

The JPL L-band synthetic-aperture radar data of figures 13 and 14 are from August 1977, taken in a single flight simultaneously. Only the image in figure 13 has been differentially rectified. In the areas of the mine dumps and tailings ponds the cross-polarized imagery is less bright than the like-polarized. This confirms an observation also made with the two polarizations of real-aperture radar (figures 6 and 7). Due to a limited geometric resolution and use of an unstabilized antenna, point targets are indistinct and boundaries are diffuse. Drainage patterns are clearly revealed by bright returns due to the low look-angle in spite of lack of sharpness and of presence of the speckle effect.

The further growth in the mining activities is evident in the images, particularly at Twin Buttes Mine (mine dumps to the west, a new structure west of Copper Mill), and at Mission Mine (mine dumps to the west and also north of Mineral Hill).

7.5. *Radar image of 1978, satellite L-band*

L-band orbital synthetic-aperture imagery acquired from the Seasat satellite was taken in August 1978 looking north-east (figures 15 and 16). Nominal range resolution is 7 m. This converts to a nominal cross-track resolution of 25 m. However, actual resolution appears to be distinctly less than the nominal value.

Image 15 is optically correlated, image 16 digitally, but neither has been rectified

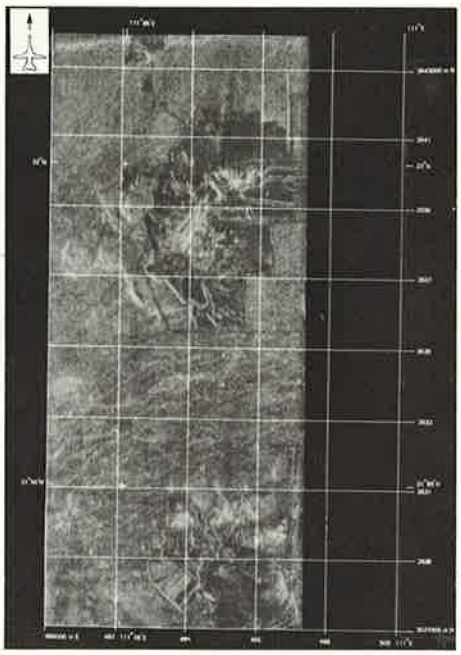

Figure 13. Synthetic aperture SLR of Jet Propulsion Laboratory (1977), rectified to UTM projection. Cross-polarized, imaging to the east. L-band (25 cm). Optical correlation.

Figure 14. Synthetic aperture SLR of Jet Propulsion Laboratory (1977), unrectified. Like-polarized, imaging to the east. L-band (25 cm). Optical correlation.

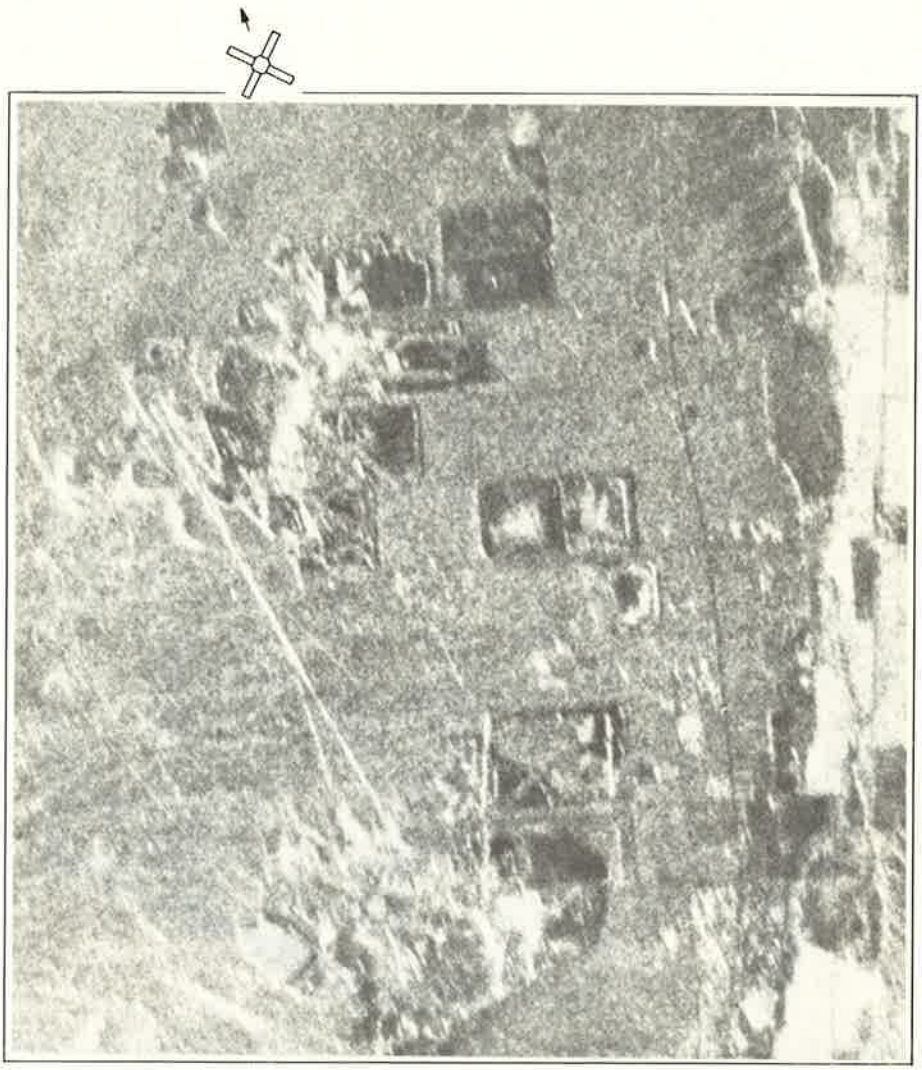

Figure 15. Synthetic aperture SLR of satellite Seasat–A (1978), unrectified. Optical correlation. L-band (25 cm).

geometrically. They contain distortions due to the combined effects of curvature and rotation of the Earth that are typical for images acquired from orbital altitudes.

Effects of speckle and low resolution combine to blur the outlines of mine buildings, dumps, ponds, roadways, etc. However, Seasat SAR image resolution and quality should be judged considering that the system was not designed for land imaging and therefore is not representative of possible satellite radar performance in this application.

In contrast with the 1973 image (figure 9) the outline of an additional tailings pond can be distinguished at the Mission Mine north of Pima Mine Road. Extremely bright returns along a line from Twin Buttes Mine to the westside of the Pima/Mission Mines probably reflect a power transmission line that does not appear on earlier images. The orientation of this line is normal to the radar look-direction. The structure

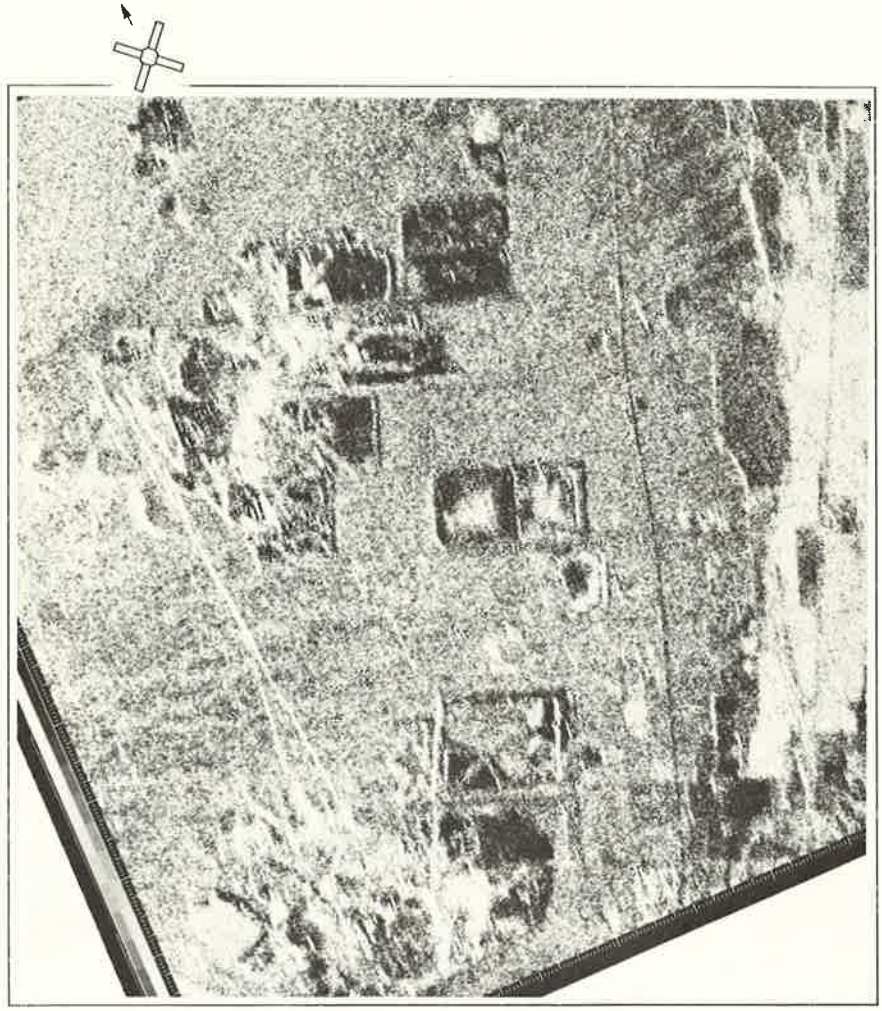

Figure 16. Synthetic aperture SLR from satellite Seasat–A (1978), unrectified; digital correlation. L-band (25 cm). Note the difference of image quality with figure 15 due to different processing of the same input data.

represented by a bright X on figures 13 and 14 at Twin Buttes Mine is scarcely discernible on figures 15 and 16. Similarly the bright point-targets that parallel the north–south routeways in figure 9 cannot be distinguished in figures 15 and 16.

Comparing optical and digital correlations (both at JPL) one does—in this example—surprisingly not encounter significant differences in interpretability due to differences of resolution or contrast. Only speckle seems to be different. Our own experiences with other Seasat data indicate that there is improved interpretability and resolution with digital correlations (see, for example, Leberl and Clerici 1980).

7.6. *Radar image of 1979, synthetic-aperture X-band*

The AN/APQ-102 (Goodyear) X-band synthetic-aperture radar is produced by the Johnson Space Center. Figure 17 is a like-polarized image, the cross-polarized is not shown. Point-target bright returns that parallel north–south routeways are on

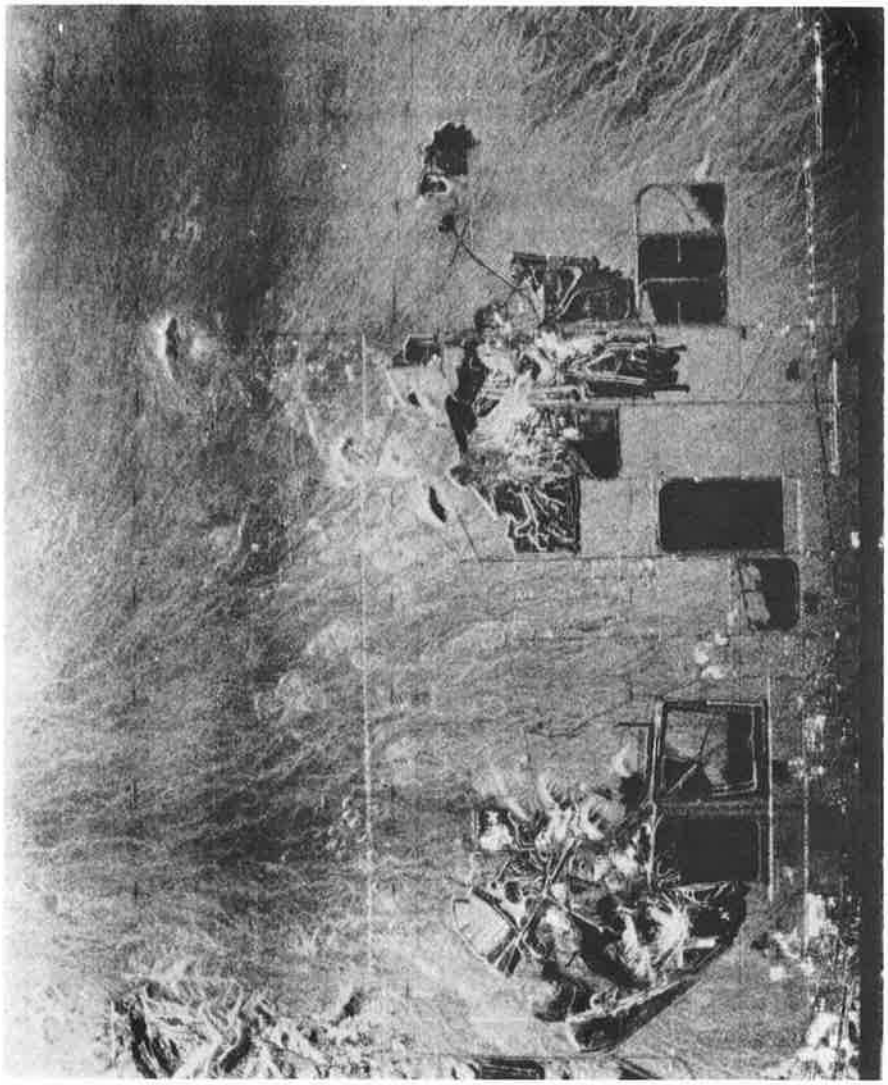

Figure 17. Synthetic aperture SLR of Johnson Space Center (Goodyear) (1979), unrectified. Cross-polarized, imaging to the west, X-band (3 cm). Optical correlation. (Courtesy Johnson Space Center.)

the like-polarized but missing from the cross-polarized image, again confirming observations from other sets of cross- and like-polarized data. The image is the latest in the series presented. In detail it is matched only by figure 9.

We find that after the Seasat pass the two adjacent tailings ponds north of Helmet Peak Road have been coalesced into one large pond; it has been built up so high that the tailings completely cover the small knoll in the eastern part of the pond (cf. figure 9).

7.7. *Radar, aerial photography, Landsat*

Since work with aerial photography and Landsat–MSS is considerably more common than with radar it may be of interest to include these image types also.

A comparison of the various radar images with aerial photography (figure 18) and Landsat (figure 19) is dominated by differences of ground resolution. With Landsat and radar, the apparently higher sharpness and image contrast of radar is not entirely due to differences in resolution (Landsat MSS pixel diameter of 80 m). Radar systems show a high sensitivity to certain point targets, to clustered buildings that act as corner reflectors and to appropriately oriented sloping topography. Thus metallic objects, built-up areas and slopes oriented normal to the radar look-direction are highlighted much more on radar than on Landsat imagery.

Aerial photography has the highest resolution and shows the greatest detail of drainage, vegetation and culture. Photographic resolution as expressed in pixel diameter may be about 2·5 m. This value is computed from an assumed 20 lp/mm resolution in the image. The conversion of lp/mm units into equivalent pixel size is based on the Kell-factor of television.

It is interesting to contrast the 1973 GEMS imagery (figure 9) with the aerial photograph (figure 18), also dating from 1973. Despite the much higher resolution of photography certain slopes and built-up areas are less distinctly presented than on radar. The drainage pipe, for example, that feeds into the centres of the tailings ponds

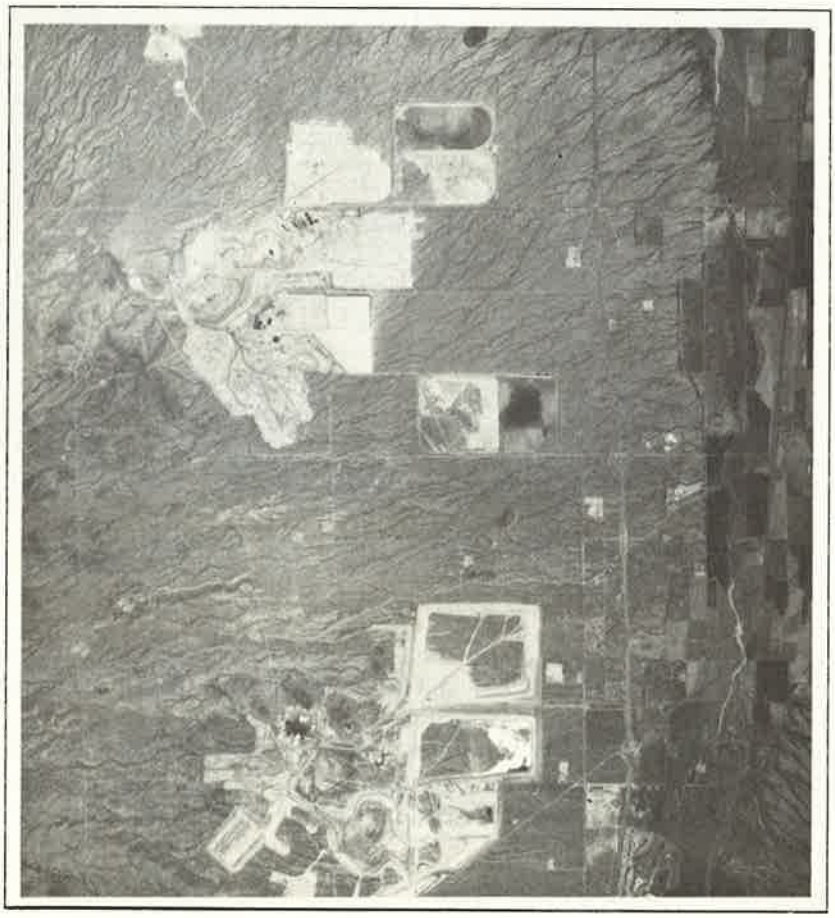

Figure 18. Section of aerial photograph, taken at scale 1:130 000 from U–2 aircraft from 20 km flight height.

north of Pima Mine Road is scarcely visible on the photograph whereas it is strongly highlighted on radar. Thus it is demonstrated that an important characteristic of imaging radar is the strong preferential enhancement that it shows for certain objects: this illustrates the difference between resolution and detectability of objects.

8. Conclusion

A unique set of ten side-looking radar images of a mining area in Arizona is presented. The objective is to demonstrate photogrammetric differential rectification as applied to radar images, and to describe the development and changes in the area over a period of nearly 15 years. To a limited extent we have used variations in look-direction, look-angle, image formation technique and polarization to illustrate the significance of these imaging parameters: low look-angles tend to emphasize variations of slope; radar sensitivity to variations in surface roughness enhances drainage channels in flat areas; high look-angles result in pronounced shadowing which enhances topography. Cross-polarized returns tend to have reduced specular effects when compared to like-polarized data. Though these facts have previously been recognized by numerous authors the data presented here are unique in that they

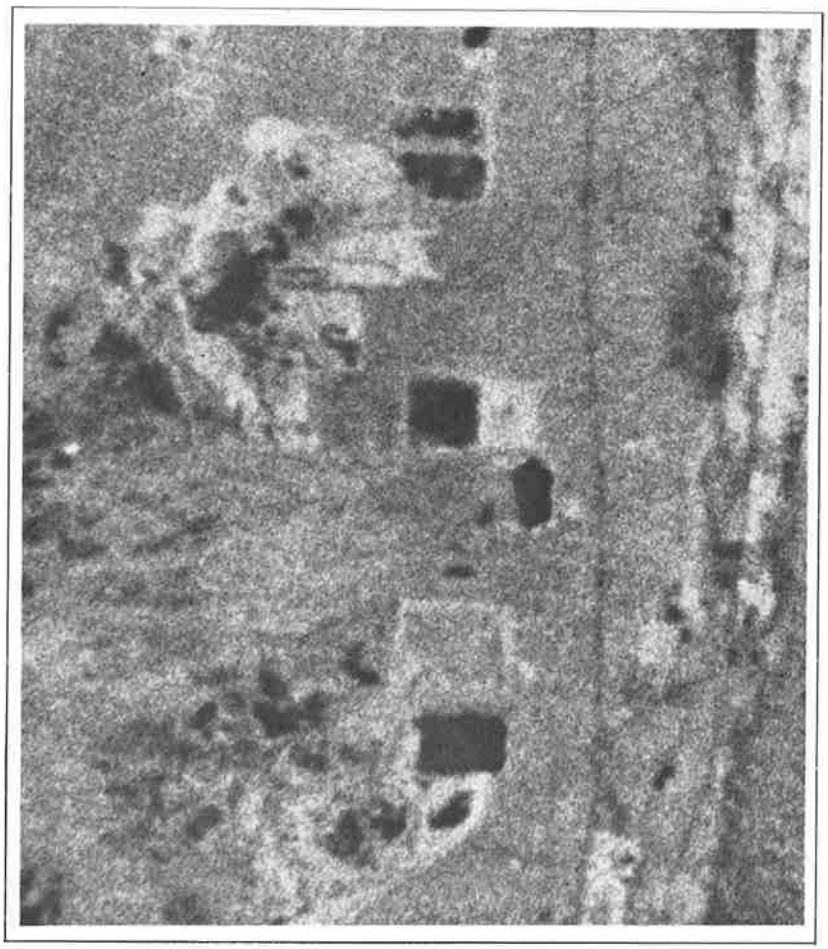

Figure 19. Section of Landsat–MSS image of channel 7 over the study area.

represent multiple coverage of a single area with a set of different radar images, aerial photography, and Landsat imagery that were acquired over a time span of 14 years.

A main result of the study consists of five differentially rectified images. Obvious budget constraints prevented us from rectification of more than only five of the available images. Remaining discrepancies of image geometry after rectification were caused by limitations in point identification. The computations to define image deformations were organized in a way enabling both optical and digital rectification. However, the procedure of rectification was applied in an optical photogrammetric machine for orthophoto-production. The cost was low for optical rectification when compared with digital image processing: about $150.00 for each of the images shown (excluding control-point measurement and deformation computation).

Any mapping effort depends on a certain metric accuracy and discipline. In the case of kinematically (dynamically) produced scan and radar imagery a high standard of accuracy is comparatively more difficult to achieve than with traditional metric photography. However, the use for thematic mapping may justify a certain relaxation of traditional photogrammetric standards. Still, we do feel that consistent data formats and presentation with grid overlays are helpful even in trivial applications such as an image time series.

Acknowledgments

We are grateful to the many agencies and individuals who provided us with image data (Aero Service–Goodyear Aerospace, Motorola Aerial Remote Sensing, NASA–JSC, EROS data center). The orthophotos were produced with the help of Professor K. Kraus of Vienna Technical University. The cooperation of J. Ford was possible under NASA Contract No. NAS 7–100 at the Jet Propulsion Laboratory, California Institute of Technology.

Appendix. Rectification technique

A 1. *Inputs to the rectification*

The procedure of rectification relies on the radar images with the following collateral data:

(*a*) ground control points;
(*b*) a digital height model,
(*c*) parameters of the flight position and antenna attitudes (exterior orientation);
(*d*) parameters of the radar system and tick marks (interior orientation).

Ground control points are identifiable points in the radar image whose coordinates in a reference system are known. For example, those coordinates may be scaled off a map.

A height model (DHM) serves to describe the topographic relief. Its purpose in the radar rectification is to help define and eliminate relief displacement in the radar image. The DHM can be derived from a topographic map, from photogrammetry, or from a previous stereo-SLR effort.

The exterior orientation should be available from flight logs, from tracking of the aircraft or spacecraft, or from recordings made during the flight or orbit. The parameters concern the sensor position with its coordinates $x(t)$, $y(t)$, $z(t)$ as a function of time t, and antenna attitude, either described by tip, $\phi(t)$, and yaw, $\kappa(t)$ for a real-aperture antenna, or by velocity components $\dot{x}(t)$, $\dot{y}(t)$, $\dot{z}(t)$ for a synthetic-aperture. Note that roll, $\omega(t)$, is not relevant.

The interior orientation encompasses a series of radar system parameters to be

known for radargrammetry. These should be time-marks to relate x_b, y_b-coordinates of each image point to a time t of imaging. Range reference and scale factors need to be known in an image so that each point can also be related to a specific slant range, r. This latter item requires the knowledge of the sweep delay, the squint angle and the sweep velocity for image recording; in the event that ground range presentations are produced the nominal flight height that was used for the ground range conversion should be known.

If any data are not available then one needs to introduce an approximate value instead; the rectification is designed to improve the approximations on the basis of ground control points.

A 2. *Image measurements and transformation*

Tick marks, distance references and all ground control points are measured in a comparator or coordinatograph. As a result one obtains cartesian x_c, y_c coordinates for each point in an arbitrary system. Using the distance reference one converts the x_c, y_c coordinates to distance and range coordinates x_b, y_b. For this an x_b-axis is defined by the points on the distance reference to pass through a straight line with coefficients a_0, a_1 (compare figure A 1)

$$y_{ck} = a_0 + a_1 x_{ck} \tag{A 1}$$

where k denotes points of the distance reference line. Using a_0, a_1 one now obtains

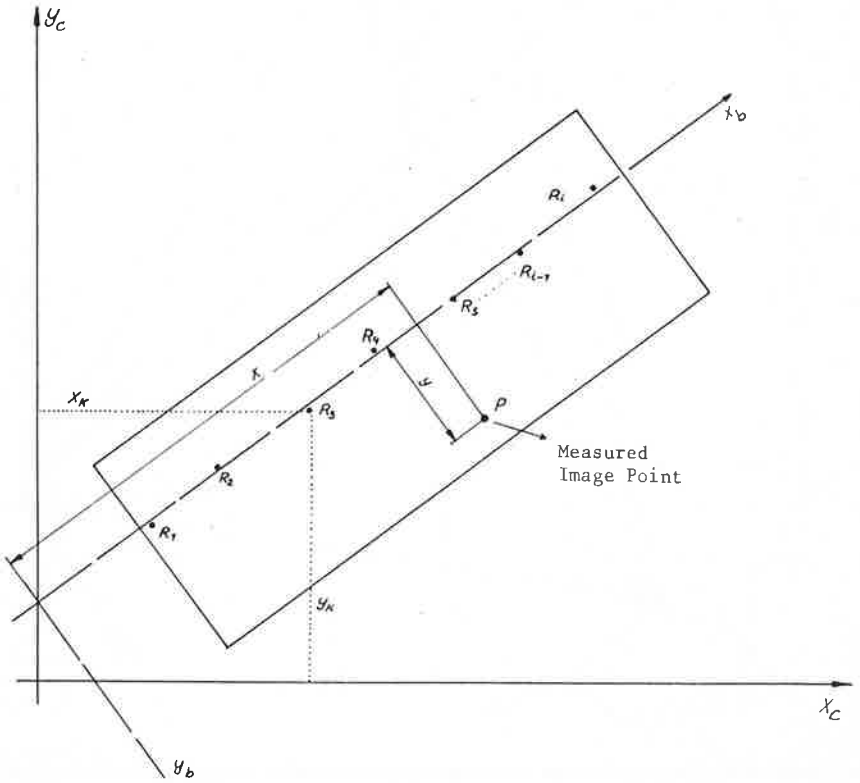

Figure A1. Coordinate systems of the comparator (x_c, y_c), and of the radar image (x_b, y_b), (after Gracie *et al.* 1970).

x_b, y_b of each image point j

$$y_{bj}=(a_1 x_{cj}-y_{cj}+a_0)/(a_1^2+a_0^2) \tag{A 2a}$$

$$x_{bj}=(x_{cj}^2+y_{cj}^2+a_0^2-2a_0 y_{cj}-y_{cj}^2)^{1/2} \tag{A 2b}$$

Provided that the slant range scale factor, f, and the constant sweep delay, c, be known, we can define the slant range, r_j, of a point j by

$$r_j=(y_{bj}+c)\cdot f \tag{A 3}$$

A 3. *Ground control points*

For each ground control point one computes the fictitious image coordinate x_b, and slant range, r, using the measured or approximate flight information and inner

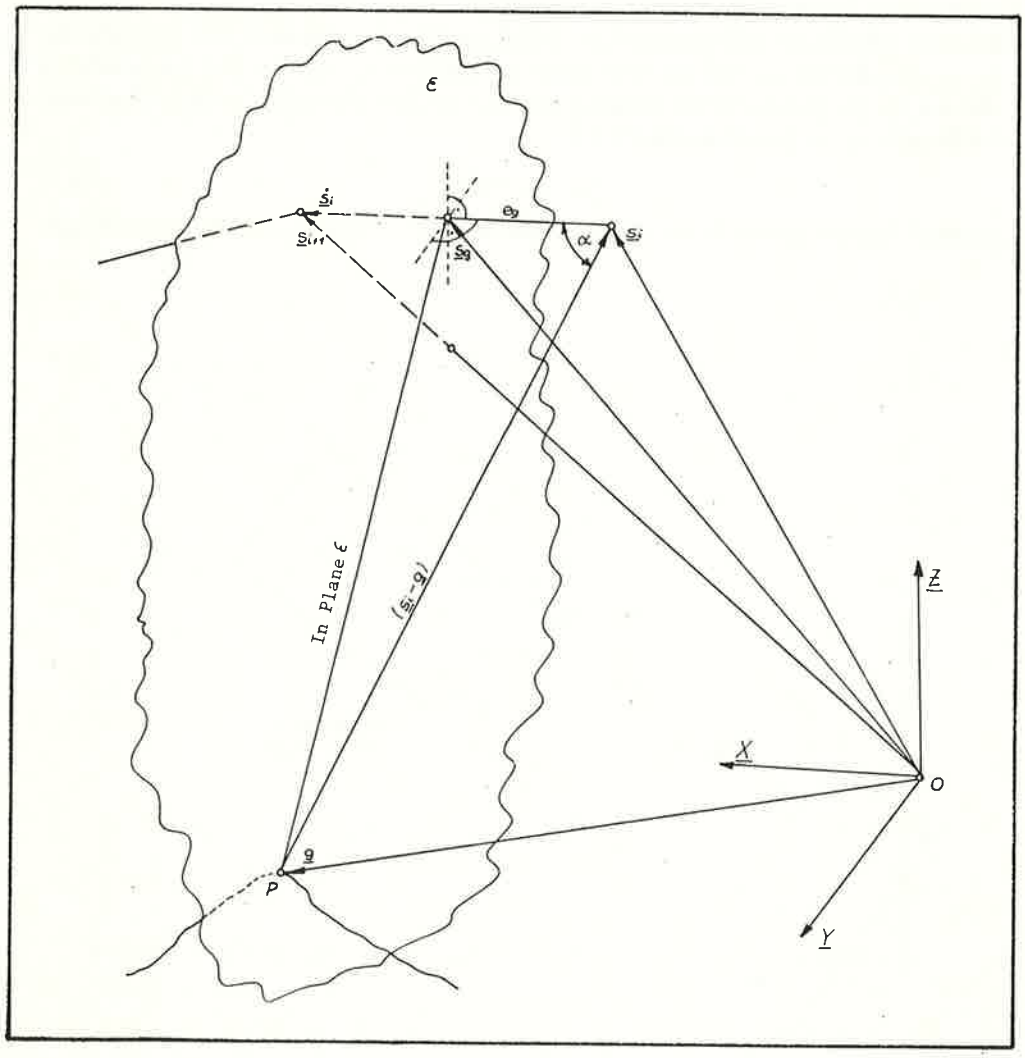

Figure A2. Computation of the flight position at which point P was imaged. Plane ε passes through P and is perpendicular to velocity vector $\dot{\mathbf{s}}$.

orientation. The procedure used was first described by Gracie *et al.* (1970) and reviewed by Leberl (1976).

Figure A 2 describes the geometric relationships using a position vector $\mathbf{s}$ of the aircraft or satellite, a velocity vector $\dot{\mathbf{s}}$, and a position vector $\mathbf{g}$ for the ground control point. The values of $\mathbf{s}$ and $\dot{\mathbf{s}}$ are known at given times, t_i, and denoted by $\mathbf{s}_i$, $\dot{\mathbf{s}}_i$. The orbit is thus represented by a succession of sensor positions that begin in location $\mathbf{s}_i$ and extend in direction $\dot{\mathbf{s}}_i$. The task is to find a plane e perpendicular to the orbit polygon and passing through a ground control point at $\mathbf{g}$. The intersection of E with the orbit is denoted by $\mathbf{s}_g$, the distance between $\mathbf{s}_g$ and $\mathbf{s}_i$ is e_g.

The problem has been formulated for synthetic-aperture radar; real-aperture radar requires a modified approach using an attitude vector. However, with rather widely spaced known platform positions or only assumed approximations one can employ the synthetic-aperture method by neglecting the difference between velocity and attitude vectors.

From figure A 2 one finds

$$(\mathbf{s}_i-\mathbf{g})\cdot\dot{\mathbf{s}}_i=|\mathbf{s}_i-\mathbf{g}\|\dot{\mathbf{s}}_i|\cos a \tag{A 4}$$

where

$$\cos a=e_g/|\mathbf{s}_i-\mathbf{g}| \tag{A 5}$$

Therefore

$$(\mathbf{s}_i-\mathbf{g})\cdot\dot{\mathbf{s}}_i=|\dot{\mathbf{s}}_i|e_g \tag{A 6}$$

$$e_g=\dot{\mathbf{s}}_i\cdot(\mathbf{s}_i-\mathbf{g})/|\dot{\mathbf{s}}_i| \tag{A 7}$$

Vector $\mathbf{s}_g$ results from

$$\mathbf{s}_g=\mathbf{s}_i+\frac{\dot{\mathbf{s}}_i}{|\dot{\mathbf{s}}_i|}e_g \tag{A 8}$$

The slant range, r, to point P, and time of imaging, t, are determined by

$$r=|\mathbf{g}-\mathbf{s}_g| \tag{A 9}$$

$$t=t_i+|\mathbf{s}_g-\mathbf{s}_i|(t_{i+1}-t_i)/|\mathbf{s}_i| \tag{A 10}$$

where t results from linear interpolation between the times t_i, t_{i+1}, at which the sensor position was measured. Actual image coordinates $\bar{x}_b$, $\bar{y}_b$ are obtained by

$$\bar{y}_b=r/f-c \tag{A 11}$$

$$\bar{x}_b=x_i+(t-t_i)(x_{i+1}-x_i)/(t_{i+1}-t_i) \tag{A 12}$$

where x_i, x_{i+1} are image coordinates belonging to times t_i, t_{i+1}. The computed image coordinates $\bar{x}_b$, $\bar{y}_b$ can now be compared with measured values x_b, y_b. This leads to discrepancies

$$\left.\begin{aligned}\Delta x&=\bar{x}-x\\ \Delta y&=\bar{y}-y\end{aligned}\right\} \tag{A 13}$$

The discrepancies can now be subjected to an interpolative correction of all non-control points. Any of a number of interpolation schemes are feasible. In the present

context of rectifying a small area we chose to use

$$\Delta x = a_0 + a_1 x + a_2 x^2 + a_3 x^3 + a_4 y + a_5 xy \qquad \text{(A 14 } a\text{)}$$

$$\Delta y = b_0 + b_1 x + b_2 y + b_3 xy + b_4 y^2 + b_5 xy^2 \qquad \text{(A 14 } b\text{)}$$

Essentially the use of polynomials in this form implies that the radar image deformations are slowly varying in the area that is considered, and that the deformations are not of a high order. These assumptions may not hold for long image strips so that spline functions must be used (Leberl *et al.* 1976).

Should imaging be done with a squint angle then the length e_g and position vector **s** in equations (A 7) and (A 8) would have to be modified. The imaging surface would not be a plane but a cone whose vertex angle is defined by squint angle τ. The modification is trivial.

A 4. *Computation of inner orientation*

It was so far assumed that the sweep delay, c, and sweep scale factor, f, were known. If this is not the case then they can be computed using ground control points. We start out from equation (A 3)

$$(y_b + c) \cdot f = r \qquad \text{(A 3)}$$

whereby y_b represents a measured image coordinate, whereas r is the slant range computed for a control point; c and f are unknown.

The equation is non-linear. Approximate values c_0, f_0 must be available to linearize

$$(y_b + c_0) f_0 + r = (y_b + c_0)\, df + f_0\, dc + v_{yb} + f_0 - v_r \qquad \text{(A 15)}$$

whereby v_{yb}, v_r are the observational errors in measuring the image coordinate y_b and slant range, r; df, dc are differential additions to the approximate values c_0, f_0. Equation (A 15) serves as an input to a least squares solution for the unknown dc, df.

After solving for df, dc, one obtains

$$c = c_0 + dc \qquad f = f_0 + df \qquad \text{(A 16)}$$

This may be carried on over several iterations, using the new c, f values as new approximations.

References

Cooley, M. E., 1973, Map showing distribution and estimated thickness of alluvial deposits in the Tucson Area, Arizona. U.S. Geological Survey, Map I–844–C.

Gracie, G., *et al.*, 1970, Stereo radar analysis. U.S. Engineer Topographic Laboratory, Fort Belvoir, Virginia, Report No. FTR–1339–1, 66 pages + Appendix.

Kobrick, M., 1980, Alien eyes. *Astronomy*, **8**, 6.

Konecny, G., 1979, Digital differential rectification. *Photogramm. Engng. Remote Sensing*, **45**, 727.

Kraus, K., 1976, Anwendungsmöglichkeiten eines digital gesteuerten Differentialumbildegerätes. Geowissenschaftliche Mitteilungen No. 8, pp. 1–22, Techn. University Vienna, Austria.

Leberl, F., 1976, Imaging radar applications to mapping and charting. *Photogrammetria*, **32**, 77.

Leberl, F., and Clerici, E., 1980, Current status of metric reduction of active scanner images. *14th Congress, International Society of Photogrammetry*, Hamburg, F.R.G. 13–26 July (invited paper). Proceedings, Vol. 23/B.3, 435–450.

Leberl, F., and Fuchs, H., 1978, Proceedings, Symposium of Comm. III of the Int. Soc. of Photogrammetry, Moscow, U.S.S.R., 30 July–5 August, 434–455.

Leberl, F., Jensen, H., and Kaplan, J., 1976, Side-looking radar mosaicking experiment. *Photogramm. Engng. Remote Sensing*, **42**, 1035–1042.

MANUAL OF PHOTOGRAMMETRY, 1966, *Combinations of Photogrammetric and Radargrammetric Techniques* (Am. Soc. Photogrammetry, Falls Church, U.S.A.), Chap. XXI.

MATTHEWS, R. E. (editor), 1975, Active microwave workshop report. NASA Special Report No. SP–376, Washington D.C., U.S.A. (502 pages).

RADAR GEOLOGY WORKSHOP, 1979, *Proceedings of a Meeting held in Snowmass*, Colorado, U.S.A. 16–21 July JPL–Publ. 80–61, JPL, Pasadena, Cal. 91103, 513 pages.

TURNER, R. M., 1974, Map showing vegetation in the Tucson area, Arizona. U.S. Geological Survey, Map I–844–H.